Published in final edited form as:
Magn Reson Med. 2008 May ; 59(5): 1062–1071. doi:10.1002/mrm.21437.

3D hyperpolarized He-3 MRI of ventilation using a multi-echo projection acquisition

James H. Holmes, PhD[1], **Rafael L. O'Halloran**[1], **Ethan K. Brodsky, PhD**[2], **Youngkyoo Jung, MS**[3], **Walter F. Block, PhD**[1,2,4], and **Sean B. Fain, PhD**[1,2]

[1]Department of Medical Physics; University of Wisconsin – Madison

[2]Department of Radiology; University of Wisconsin – Madison

[3]Department of Electrical and Computer Engineering; University of Wisconsin – Madison

[4]Department of Biomedical Engineering; University of Wisconsin – Madison

Abstract

A method is presented for high resolution 3D imaging of the whole lung using inhaled hyperpolarized (HP) He-3 MR with multiple half-echo radial trajectories that can accelerate imaging through undersampling. A multiple half-echo radial trajectory can be used to reduce the level of artifact for undersampled 3D projection reconstruction (PR) imaging by increasing the amount of data acquired per unit time for HP He-3 lung imaging. The point spread functions (PSFs) for breath-held He-3 MRI using multiple half-echo trajectories were evaluated using simulations to predict the effects of T_2* and gas diffusion on image quality. Results from PSF simulations were consistent with imaging results in volunteer studies showing improved image quality with increasing number of echoes using up to 8 half-echoes. The 8 half-echo acquisition is shown to accommodate lost breath-holds as short as 6 s using a retrospective reconstruction at reduced resolution as well as to allow reduced breath-hold time compared to an equivalent Cartesian trajectory. Furthermore, preliminary results from a 3D dynamic inhalation-exhalation maneuver are demonstrated using the 8 half-echo trajectory. Results demonstrate the first high resolution 3D PR imaging of ventilation and respiratory dynamics in humans using HP He-3 MR.

Introduction

Obstructive lung disease is highly heterogeneous (1), requiring 3D coverage at sufficient resolution to detect loci of disease. Hyperpolarized gas (HP) He-3 MRI with 3D isotropic resolution will likely improve depiction and analysis of lung structures and ventilation defects by reducing partial volume effects and providing true cubic voxel size for segmentation and measurement. However, challenges remain as the polarization is non-recoverable and sampling time is limited by the breath-hold duration.

HP He-3 imaging has been performed using non-Cartesian 2D trajectories such as spiral (2) and undersampled projection acquisition to allow depiction of HP He-3 in the lungs using short breath-holds (3,4,5,6). These techniques provide a method of detecting regional ventilation differences without the use of ionizing radiation associated with CT (7). Breath-held spin-density imaging of the lungs in 3D has been demonstrated using Fourier techniques (8), stack of spirals (9), and cyclindrical techniques (10). The use of functional

Correspondence and reprint requests: Sean B. Fain, J5/M150 CSC Medical Physics Box 1590, 600 Highland Avenue, Madison, WI 53792, Phone 608 263-0090; Fax 608 265-9840; sfain@wisc.edu.

HP He-3 data has shown exciting prospects in the setting of radiation treatment planning for lung cancer where 3D isotropic data will aid in registering anatomic with functional images of the lungs (11). A 3D stack of stars acquisition comprised of undersampled 2D projection acquisition in-plane and Fourier encoding in the third dimension has also been demonstrated to provide improved 3D visualization for short breath-holds as well as detection of gas trapping (6). However, each of these methods has tradeoffs with respect to spatial and temporal resolution as well as sensitivity to motion for depiction of dynamic processes, complex lung structure, and accommodating loss of breath-hold during the acquisition.

A fully 3D projection acquisition trajectory and projection reconstruction (PR) has advantages for HP He-3 lung imaging as it allows the flexibility to not only perform spin-density imaging at isotropic resolution, but also to acquire functional information about the lungs including dynamic images due to the frequent resampling of the center of k-space. Angularly undersampled PR has been demonstrated for acceleration of data acquisition in high contrast to noise (CNR) applications (12). Multi-echo projection techniques using gradient echo acquisition have been shown for further improved data collection efficiency in high temporal applications such as cardiac imaging and MR fluoroscopy (13,14). In addition to the angular undersampling opportunities of PR, these methods reduce the number of excitations needed allowing a greater percentage of total acquisition time be spent collecting data. Vastly undersampled isotropic projection acquisitions (VIPR) have been demonstrated to allow high spatial resolution imaging of dynamic processes at the cost of streak artifacts (15). Fully 3D PR has advantages for imaging large volumes in angiography applications. Additionally, a modification of the standard projection acquisition trajectory has been shown using multiple echoes and bent projections (VIPR-ME) to improve the angular sampling and signal to noise ratio (SNR) efficiency ($\mathrm{SNR}/\sqrt{\text{scan time}}$) when going from a radial (1 half-echo) to a 4 half-echo trajectory (16). In contrast enhanced angiography, the use of an 8 half-echo VIPR trajectory has been demonstrated to improve data collection efficiency for time-resolved studies in the pulmonary vasculature (17). These improvements in data collection efficiency are particularly applicable to HP lung imaging where only limited breath-hold times are possible and there is only a limited supply of prepared magnetization for imaging.

One of the unique features of imaging HP species is that the magnetization is non-recoverable and therefore the available magnetization in the longitudinal plane can vary greatly with each RF excitation. Work has been presented, looking at signal modulations with RF flip angle in imaging of nuclear species with long T_1 values (18,19,20,21). Further, the affects of modulating the flip angle in HP gas imaging has also been demonstrated (22,23,24,25,26) as well as in projection acquisition of respiratory gated small animal studies (27).

Because the HP gas polarization is non-recoverable, it is desirable to maximize the SNR efficiency and k-space coverage while minimizing signal loss due to RF depletion of the longitudinal magnetization (M_z) for successive RF excitations. Additionally, rapid image acquisition is desirable to accommodate limited breath-hold times. Undersampled 3D PR, having advantages in high CNR settings with respect to SNR efficiency, may be well suited to the high CNR environment and limited acquisition times encountered in HP gas imaging. The hypothesis of this work is that multi-echo 3D PR can provide sufficient SNR efficiency to reduce under-sampling artifact and enable high resolution 3D imaging during short breath-holds as well as respiratory dynamics.

Methods

The necessary number of projections to meet the Nyquist criterion in three dimensions is:

$$n_p = \frac{\pi}{2} n_r^2 \quad [1]$$

where n_p is the number of projections and n_r is the readout resolution along a projection. Details of the angularly undersampled 3D VIPR and the multi-echo VIPR-ME techniques have previously been published (15,16). For the multi-echo PR acquisitions in both numerical simulations and volunteer studies detailed in this work, the method for selecting projection angles along the 3D sphere of k-space was based on a spiral trajectory (28). Ordering of the projection angles was then performed such that the angles were sequentially incremented within a single TR. Further, the projection angle set was broken into several subsets (interleaves) of evenly spaced angles, each interleave distributed over the entire sphere of k-space much like a cine-type acquisition.

Numerical Simulations

Multi-echo PR imaging in the presence of T_2* decay can result in two effects that degrade image quality. The first effect is blurring within a single projection due to signal dephasing across the data readout. The inter-projection blurring is related to the time required to traverse k-space in a single echo and the T_2* decay time. If the T_2* decay within a single projection angle is significant, it can result in loss of resolution and is typically modeled as a blurring kernel in image space. The second effect from T_2* is the difference in signal between different angular projections. Large differences in signal from one projection to the next can be modeled as an undersampling effect where the image quality becomes dominated by the projections with the largest intensity. An added complication in gas imaging is the large coefficient of diffusion. The use of large readout gradients for rapidly traversing k-space can also result in diffusion weighting of the data.

Due to these features of multi-echo PR imaging, acquisition trajectories need to be designed to maximize data collection efficiency, while limiting time spent not collecting data or collecting corrupted data that can lead to loss of image quality. Numerical point spread function (PSF) simulations were performed to objectively compare different multi-echo 3D PR trajectories for HP He-3 lung imaging targeting a 20 s breath-hold. Specifically, k-space data were synthesized including signal attenuation due to RF depletion, T_2*, and diffusion on a point-by-point basis to model the signal modulations for physical parameters discussed in the volunteer and phantom imaging section below.

The simulated k-space data were then regridded and density compensation filtering was performed to account for the spatially varying sampling density. Finally, zero-filling was performed to allow interpolation up to a 512^3 matrix size and a 3D FFT was applied to determine the PSF. The PSFs for the 1 half-echo, 2 half-echo, 4 half-echo, and 8 half-echo trajectories were compared for total signal by measuring the maximum amplitude of the central peak in the PSF and for resolution by measuring the full-width-at-half-maximum (FWHM). Qualitative measures of the PSFs were made for the radius of the supported field of view (FOV). The supported FOV was evaluated using radially averaged plots of the PSF normalized to the same peak height and depicted using a $\sqrt[4]{magnitude}$ transform to aid in visualization of the lower signal regions. An idealized diagram of the trajectory in k-space and the pulse sequence diagrams for both a 1 half-echo and a 4 half-echo acquisition is shown in Figure 1 demonstrating the improvement in data collection efficiency with increasing number of echoes. Note that times for the RF pulse and spoiler gradients are constant for both trajectories but more of the total TR time can be spent performing data collection during the 4 half-echos, thus improving the data collection efficiency and reducing the number of RF pulses needed for equivalent angular sampling.

Simulations were performed for the conventional excitation method in HP He-3 MRI using a small constant RF flip angle. These included simulations to determine the optimal constant flip angle providing the greatest maximum amplitude in the central peak or the PSF. In addition, the conventional excitation method was compared with a modulated flip angle that transfers a constant amount of magnetization into the transverse plane with each RF pulse to mitigate signal modulations. For a total of N RF pulses, the modulated RF flip angle θ_i for the i^{th} RF pulse was calculated using equation 2 (Ref. 23).

$$\theta_i = \text{atan}\left(\frac{1}{\sqrt{N-i}}\right) \quad [2]$$

The T_1 decay of the HP He-3 polarization due to oxygen within the lungs was not included as it was considered to be of less relevance for comparing different multi-echo trajectories within a fixed breath-hold time.

As the T_2* and level of restriction for gas diffusion are different for the lung alveoli compared to the larger airways, PSF simulations were performed to evaluate the different multi-echo trajectories for both regions of the lungs. Simulations were performed for both the larger airways assuming a T_2* of 18.5 ms and gas diffusion coefficient of 0.8 cm^2/s, as well as for the alveolar gas spaces assuming a T_2* of 7.9 ms and diffusion coefficient of 0.2 cm^2/s based on typical values in the literature (29). Bent projections were used to further improve the azimuthal sampling density and the data were reconstructed using homodyne synthesis to exploit the symmetry of k-space to further accelerate the data acquisition (30,31).

Volunteer Imaging Studies

Phantom and volunteer studies were performed to validate the simulation results. A normal volunteer was imaged after informed consent using the 2, 4, and 8 half-echo trajectories with a modulated RF flip angle as well an 8 half-echo trajectory with a constant flip angle. Doses of 5.6 mM of HP He-3 mixed with N_2 gas were inhaled during each acquisition to facilitate comparison of image quality between acquisition trajectories. Imaging was performed on a 1.5T Signa HDx clinical scanner equipped with an EchoSpeed gradient system and broadband capability (GE HealthCare, Milwaukee, WI). A transmit/receive vest coil tuned to ~48 MHz (the resonant frequency of He-3 at 1.5 T) was used (Medical Advances, Milwaukee, WI). He-3 gas was polarized to levels of 30–40% using spin-spin exchange with optically excited Rubidium vapor (GE HealthCare, Milwaukee, WI). A fast spoiled gradient recalled (SPGR) acquisition that included RF spoiling in addition to the normal gradient spoiling was used for imaging and scan parameters included a cubic FOV of 42 cm in each dimension, BW = ± 125 kHz, and 200 μs nonselective RF pulse. The maximum gradient amplitude during the studies was 18.3 mT/m. As with the numerical simulations, bent projections were employed. The key imaging parameters used in the simulations are summarized in Table 1. The 2 half-echo acquisition acquired 16,320 half-angle projections while the 8 half echo trajectory acquired 35,200 half-angle projections in the same breath-hold time. For comparison, a minimum of 25,736 projection angles (51,472 half-angle projections) are required to satisfy the Nyquist criterion. To improve sampling efficiency and further minimize the echo time, ramp sampling was performed. The maximum radial distance from the center in k-space corresponded to 64 evenly spaced points on a Cartesian grid. The gradient waveforms and timings of the 1 half-echo (radial outward) acquisition were identical to the 2 half-echo acquisition however data acquired during the rephaser gradient (2^{nd} half-echo) was discarded.

The modulated RF flip angle discussed in the numerical simulations was utilized for imaging experiments comparing each of the multi-echo trajectories described above. Also for comparison, an imaging experiment using the optimal constant ~1.35° flip angle determined from the PSF simulations was performed using the 8 half-echo trajectory. To compensate for cardiac motion as well as nonlinearities in the RF amplifier, 10 of the unique interleaved angle sets were acquired, each set covering the full sphere of k-space as described above. This interleaved acquisition also helps to distribute motion and any uncorrected signal modulation due to RF depletion of M_z and T_1 decay of the gas. These RF effects are particularly important in PR imaging in which signal modulations lead to an increased angular under-sampling artifact in the image.

Breath-hold spin density imaging studies were reconstructed by regridding onto a 128^3 Cartesian cube then zero-filling to a 256^3 matrix size. Data acquired for each TR during the gradient ramps and plateaus were regridded. However, the data points acquired during the tangential blips, used to make small angle changes at the outer radius of k-space, were discarded. As with the numerical simulations, all data were reconstructed using homodyne synthesis. Quantitative measures of signal to noise ratio (SNR) were made in the large airways and the alveolar gas spaces of the lungs to compare expected signal losses due to diffusion and T_2* with the simulation results. The aliasing from angular undersampling was found to vary spatially due to the structure of the lungs and trachea. For this reason, several ROIs were averaged from outside the lungs as well as inside the signal void of the heart.

Time subsets of data (comprised of one or more interleaved angular set) for the 8 half-echo acquisition were reconstructed to demonstrate the capability of imaging over shorter breath-holds compared to the full 20 s breath-hold. For example, to simulate a breath-hold lasting only 8 s, the first 8 s of data were reconstructed and the remaining 12 s were not used. Shortened breath-hold images were also reconstructed to the same matrix size of 256^3 using homodyne synthesis. Data were spatially filtered using a density compensating filter that minimizes the least square error in the reconstruction rather than maximizing the spatial resolution (32). Data were reformatted to produce axial, coronal, and sagittal views using 3.3 mm thick limited MIPs (maximum intensity projections).

A dynamic study was performed using the 8 half-echo trajectory to image a volunteer during a 40 s inhalation and forced exhalation maneuver. To enable better depiction of dynamic processes, 40 unique interleaved angle subsets were acquired where each interleaved set required 1 s of acquisition time. To compensate for angular undersampling in the dynamic data, a sliding window reconstruction was performed using a temporal filter that varies radially in k-space (tornado filtering) (15). The base of the tornado filter at low spatial frequencies was 2 s and the width at the top of the filter at the high spatial frequencies was 6 s. As with the short breath-hold simulations, a density compensating filter was applied. Dynamic time frames were reconstructed to a 256^3 matrix. To demonstrate the 3D nature of each time-frame; axial, coronal, and sagittal reformats of this data were positioned to track the same physical structures in the lungs at 4 key time-points using limited 1.3 cm thick MIPs.

Spatially registered anatomic proton and He-3 MRI with matched lung volumes were acquired using the 4 half-echo acquisition. Scan parameters for the proton MRI were TR/TE of 2.9 ms / 0.21 ms with the same scan location, FOV, and voxel size as the He-3 dataset, making the two datasets inherently co-registered. Following volunteer imaging, gradient calibration acquisitions were performed on a water phantom placed at isocenter in the MR scanner, to be discussed in the following text. Data were reconstructed on a 256^3 matrix.

Gradient deviations leading to errors in the desired k-space trajectory were corrected using the technique outlined by Duyn et al. (33) and demonstrated for the VIPR-ME trajectory (16). The trajectories on each of the physical gradient axes were independently measured and contributions due to gradient delays and eddy currents were calculated. Corrections to trajectories using arbitrary angles off of the physical gradient system axis were calculated using linear interpolation of the trajectories measured on each physical axis. The isotropic delay between the gradient systems and the RF chains were approximately the same for both the primary and the broadband paths but the effects due to eddy currents were found to vary over the course of the day due to gradient system heating and other possible causes (34).

Measuring the k-space trajectory deviations in a patient during a breath-hold of HP He-3 is difficult due to gas availability and the geometry of the lungs. For these reasons we developed a system to measure the trajectory using a proton phantom. A tedlar bag (Jensen Inert, Coral Springs, FL) of HP He-3 mixed with N_2 gas was imaged to demonstrate the calibration process because the gas concentration (and therefore the He-3 signal) should be constant throughout the volume. Figure 2 demonstrates the calibration process. First, trajectory measurements along the physical gradient axis were made using the standard proton RF chain. In these studies, a standard proton head phantom (GE HealthCare, Milwaukee, WI) was used, however the technique is not strongly dependant on the phantom geometry. The trajectory measurements were then used to form a k-space correction map of the actual position of each data point in k-space for the empirical gradient wave forms of the acquisition. The k-space correction map was then applied to the He-3 data acquired using the same gradient trajectory, in this example a bag of He-3 and N_2 gas. Effective gradient delays of 1.8, 3.6, and 4.4 μs were measured on the physical x, y, and z gradient axes respectively on the specific MRI scanner used for imaging studies. Signal dropout in the He-3 image is visible near the periphery of the bag phantom and signal is also distributed outside of the bag in the un-corrected data (Figure 2). By comparison, the corrected He-3 data show relatively uniform signal intensity inside the gas bag with better suppression of background signal. This process allowed for correction of the He-3 data, based on trajectory measurements made using the standard proton RF chain.

Results

Numerical Simulations

The maximum amplitudes of the central peak in the PSFs were measured and are summarized in Table 2. The 8 half-echo trajectory is shown to provide greater signal collection demonstrated by the larger maximum amplitude of the central peak in the PSF over the other trajectories using both the modulated as well as the constant flip angle. Furthermore, the modulated flip angle was found to produce a larger maximum amplitude than the optimal constant flip angle. The constant flip angles producing the maximal PSF peaks for each of the four trajectories were found to correspond to the use of ~70% of the initial magnetization for the simulation parameters used in this study. Simulations for the lung alveolar gas spaces for 1 half-echo (radial trajectory) show that the PSF maximum amplitude with and without T_2* decay and diffusion are very similar (within 3–7 %). This demonstrates that the 1 half-echo trajectory is largely limited by the number of radial lines that can be sampled in 20 s. Although the absolute amplitude is substantially greater, the 8 half-echo trajectory results in a greater percentage decrease in the maximum amplitude of the central peak in the PSF due to the effects of T_2* and diffusion (13–21 %). This demonstrates the expected tradeoff between increased sensitivity to T_2* and diffusion and the benefit of the additional radial lines sampled through the acquisition of more half-echos.

The PSF analysis also shows that even in the presence of T_2* decay and diffusion, there is relatively little change in the side-lobe regions even for the 8 half-echo trajectory compared

to the trajectories acquiring fewer echoes (Figure 3). In the absence of attenuation of signal due to RF, T_2* or diffusion, there is an increase in the supported FOV as the number of collected half-echos increases as expected (Figure 3 a). Once signal attenuation due to RF depletion, T_2*, and diffusion are included, simulation results for large airways and the alveolar gas space show the supported FOV also increases with increasing number of echoes with some contamination of the side-lobe energy within the supported FOV (Figure 3 b, c). Results for the PSFs using the modulated flip angle similarly show a larger supported FOV for the 8 half-echo acquisition while there is less evidence of side-lobe contamination after including T_2* and diffusion effects (Figure 3 d e). The FWHM of the PSFs for all simulations were measured to be 1.50* Δx, where Δx is the initial voxel size, and any blurring due to RF, T_2*, or diffusion was below the level of detection. The modulations in PSFs due to T_2* decay and diffusion at later echo times were found to be negligible for the multi-echo acquisition schemes due to the moderate data acquisition time interval used for the simulation parameters used. The simulation results predicted that the 8 half-echo trajectory should provide improved image quality for HP He-3 lung evaluation compared to the 1, 2, and 4 half-echo trajectories.

Volunteer Imaging Studies

Volunteer studies (Figure 4) corroborated the PSF simulations showing that SNR and image quality increased with the number of half-echoes acquired up to a maximum of 8. Consistent with the simulation results, the SNR measured in both the trachea and the alveolar gas spaces were found to be the highest for the 8 half-echo acquisition (Table 2). Contrary to the simulation results, the volunteer studies comparing the modulated and constant flip angle acquisitions with the 8 half-echo trajectory showed modestly improved SNR for the constant flip angle acquisition.

To demonstrate the capability of imaging over breath-hold times less than 20 s, subsets of data from the exam using an 8 half-echo trajectory and a modulated flip angle were retrospectively reconstructed. Individual axial images from the 3D data are shown for the full 20 s breath-hold, the first 10 s, and down to only 6 s of the breath-hold (Figure 5). Major features of the entire 3D lung ventilation, including the large airways and the regional variations in the alveolar gas spaces, are visible even in the images from the shortest (6 s) breath-hold time. These results demonstrate the capability of retrospectively reconstructing a subset of the data if a subject is unable to maintain their breath-hold prior to completion of the entire 20 s acquisition. While loss of spatial resolution due to the density compensation filtering in k-space is evident in the shortest breath-hold reconstructions, the basic structures are well preserved.

Results from the dynamic study (Figure 6) depict no signal present in the lungs at the start of the acquisition prior to inhalation of the gas. From 4–6 s, HP He-3 is visible entering the large airways followed by alveolar gas space enhancement from 7–9 s. A short breath-hold was performed from 10–21 s. Afterwards a forced exhalation is performed and upward motion of the diaphragm and loss of signal in the trachea are shown from 22–25 s. Following the forced exhalation, the subject maintained this position for a short time 26 s. Axial, coronal, and sagittal 13 mm thick limited MIP images are shown for 4 of the time frames to better demonstrate the 3D nature of the data (Figure 7). Although increased streak artifact is apparent, filling of the airspaces is well visualized including the large airways at 6 s, parenchymal enhancement at 9 s, and the breath-hold phase at 15 s. Following the forced expiration maneuver, a decrease in lung volume is evident as residual gas remaining in the lung depicts that the diaphragm has moved upward and the chest wall has moved inward (25 s). There is decreased signal in the right middle lobe suggestive of delayed filling (9 s) and a ventilation defect (15 and 25 s) (Figure 7 arrows).

Images from a reformatted and co-registered He-3 ventilation and proton dataset acquired using the 4 half-echo trajectory for 20 s breath-hold times are shown in Figures 8. Each image depicts a 1.64 mm thick partition of the 3D volume. The proton data can provide information about the anatomic structure of the lungs including the lung borders and regions of dense tissue infiltrate. Fusion images of the ventilation and anatomic structure allow improved visualization of the lung periphery and pulmonary vasculature. Results show correspondence of He-3 ventilation (red) and proton anatomy (blue) (Figure 8 a, d, g) depicting overlap of ventilation in the lung as well as ventilation voids in the pulmonary vasculature. A difference in the He-3 signal intensity is visible in the left lobe. This feature correlates to the septation between the upper and lower lobes and is likely due to a difference in ventilation (Figure 8 a, b, c arrows). Also, note that the septation of the individual lobes in the right lung (Figure 8 g, h, i arrows) are visible in the fused data and the He-3 ventilation image but are not in the anatomic dataset.

Discussion and Conclusions

The multi-echo PR method provides full coverage of the lungs at isotropic voxel size for breath-held studies while maintaining image quality if the subject is unable to complete the entire breath-hold. Furthermore, these advantages are extended to 3D dynamic imaging of the lungs and preliminary results are presented. Simulation and volunteer studies for breath-held imaging were performed to optimize the k-space trajectory, taking into consideration T_2* decay, diffusion, RF depletion, and breath-hold time. These results showed that for 3D PR imaging of HP He-3 gas in the lungs, data sampling efficiency is the primary limitation on image quality in applications demanding limited breath-hold times. Therefore, the improved data collection efficiency of multi-echo PR and the ability to angularly undersample the data to accelerate the acquisition allows the breath-hold to be shortened by roughly half that of a fully sampled Cartesian trajectory at equivalent voxel size and FOV. Further, in case of the loss of breath-hold, 3D imaging of the lungs can still be achieved within as little as 6 s if necessary. Cartesian acquisition methods would likely fail in the circumstance of lost breath-hold and could not be as readily adapted to accommodate a range of breath-hold times depending on the subject's ability to cooperate. This ability of 3D PR to accommodate unexpected loss of patient breath-hold may provide significant advantages in making these methods more practical for clinical use and particularly in imaging children or individuals with severe lung disease.

Furthermore, the isotropic voxel size facilitates accurate co-registration of proton images of anatomic structure with He-3 images of ventilation. Reformatting these images into arbitrary planes can provide better depiction of ventilation as well as improved sensitivity to abnormalities in the lung. This may be particularly useful for the lung transplant setting as well as in lung cancer radiation dose treatment planning where HP He-3 has recently been demonstrated (11).

In theory, the modulated flip angle method has the advantage of maximizing the use of the available finite HP magnetization, while providing constant transverse magnetization for the beginning of each TR compared to the constant flip angle method. However, although the PSF simulations support the expected improvement with the use of a modulated flip angle, the constant flip angle performed modestly better in volunteer studies. This may be due to sub-optimal coil homogeneity, non-linearity in the RF amplifier performance, oxygen related T_1 decay of the gas within the lungs, as well as differences in the volunteer's lung volume prior to HP gas inhalation.

The use of multi-echo PR trajectories for imaging very short T_2* species relative to the readout time can result in significant dephasing of signal during a single projection and loss

of spatial resolution. In cases of more moderate T_2* values relative to the readout time, each echo samples a unique angle of k-space and therefore later echoes will contribute less signal. If sufficient numbers of echoes are acquired, the resultant PSF can begin to approximate an angularly under-sampled data space. However, in this work the loss of signal due to T_2* results in negligible loss of image quality for the T_2* values found in the lungs due to the rapid readout times used for these PR trajectories. Within a single TR, the read-out gradients from previous half-echoes can result in some diffusion weighting of later half-echoes. While this diffusion weighting is not significant for typical proton imaging applications, the diffusion contribution is non-trivial for gas imaging. The use of ramp sampling limited the *b*-value from the imaging gradients to 0.13 s/cm^2 at the 8th half-echo. This corresponds to an estimated signal attenuation of 3 % in the alveolar gas spaces and 12 % in the high diffusion regions of the trachea and larger airways during the last echo. However, despite the T_2* and diffusion related signal losses, the increased data collection efficiency provided by the 8 half-echo acquisition was still found to provided the greatest improvement in both PSF and image quality.

The experiments in this study suggest that improvements in image quality observed for the 8 half-echo trajectory are primarily due to reduction of undersampling artifact. However, there remain unexplained signal decreases in the alveolar gas space when comparing 4 to 8 half-echo acquisitions not predicted by the simulations. The signal loss is most likely the result of deviations in k-space trajectory due to uncorrected gradient imperfections or greater than expected T_2* decay. In particular, errors in regridding the low-spatial frequency data can result in drop-off of signal toward the edges of the lung. The deviations due to eddy currents were empirically found to drift and calibration data was acquired close in time to the imaging study to minimize differences between the trajectory map and the MRI gradient system configuration. The gradient calibration data was acquired in a water phantom a short time after the volunteer imaging was performed and the trajectory errors may have changed between these time-points due to temperature changes in the gradient systems. Performing the gradient calibration using a proton acquisition directly on the volunteer prior to HP He-3 imaging will mitigate these errors.

Future work will further explore the use of the 3D PR multi-echo technique for dynamic imaging of respiration and gas trapping. The passage of each PR trajectory through the center of k-space has been used to depict the contrast kinetics associated with inspiratory and expiratory dynamics in three dimensions. It is expected that this application may be challenging due to limited SNR, therefore we have applied the view-sharing temporal (tornado) filtering technique in this work to decrease angular undersampling artifacts. However, recent advances in projection reconstruction for time-resolved data (35,36) may allow significantly improved image quality for 3D dynamic imaging of gas respiration. Additional studies will also look at further optimization of the total acquisition time and flip angle dependencies for projection imaging.

In summary, isotropic high resolution 3D ventilation imaging using multi-echo PR was demonstrated. Although 3D spiral trajectories (37) may also allow improved SNR efficiency for HP gas lung imaging, multi-echo PR provides greater flexibility for time resolved applications including imaging of dynamic respiration and gas trapping in 3D. Further optimization of the number of excitations, k-space trajectory, and RF flip angle, will improve image quality and may facilitate extension of the technique to other applications, such as 3D diffusion-weighted HP gas MRI and oxygen-mapping (38,39,40). Future work will include the application of multi-echo PR imaging to the study of disease including lung cancer and asthma.

Acknowledgments

This work was supported by: a Hartwell Foundation Fellowship to JHH, NIH Grant 2P50-HL56396-06, NIH Grant 2T32-CA09206-26, and an award to SBF from the Sandler Program for Asthma Research, GE Healthcare.

References

1. Samee S, Altes TA, Powers P, de Lange EE, Knight-Scott J, Rakes G, Mugler JP, Ciambotti JM, Alford BA, Brookeman JR, Platts-Mills TA. Imaging the lungs in asthmatic patients by using hyperpolarized helium-3 magnetic resonance: assessment of response to methacholine and exercise challenge. J Allergy Clin Immunol 2003;111:1205–1211. [PubMed: 12789218]
2. Salerno M, Altes T, Brookeman J, de Lange E, Mugler J III. Dynamic spiral MRI of pulmonary gas flow using hyperpolarized 3He: preliminary studies in healthy and diseased lungs. Magn Reson in Med 2001;46:667–677. [PubMed: 11590642]
3. Schreiber WG, Weiler N, Kauczor HU, Markstaller K, Eberle B, Hast J, Surkau R, GroBmann T, Deninger A, Hanisch G, Otten EW. Ultraschnelle MRT der Lungen-ventilation mittels hochpolarisiertem Helium-3. Fortschr Rontgenstr 2000;172:129–133.
4. Wild JM, Paley MNJ, Kasuboski L, Swift A, Fichele S, Woodhouse N, Griffiths PD, van Beek EJR. Dynamic radial projection MRI of inhaled hyperpolarized 3He. Magn Reson Med 2003;49:991–997. [PubMed: 12768575]
5. Koumellis P, van Beek EJ, Woodhouse N, Fichele S, Swift AJ, Paley MN, Hill C, Taylor CJ, Wild JM. Quantitative analysis of regional airways obstruction using dynamic hyperpolarized 3He MRI - Preliminary results in children with cystic fibrosis. J Magn Reson Imaging 2005;22:420–426. [PubMed: 16104046]
6. Holmes JH, Korosec FR, Du J, O'Halloran RL, Sorkness RL, Grist TM, Kuhlman JE, Fain SB. Imaging of lung ventilation and respiratory dynamics in a single ventilation cycle using hyperpolarized He-3 MRI. J Magn Reson Imaging. 2007 online August 8.
7. Gast KK, Viallon M, Eberle B, Lill J, Puderbach MU, Hanke AT, Schmiedeskamp J, Kauczor HU. MRI in Lung Transplant recipients using hyperpolarized 3He: comparison with CT. J Magn Reson Imaging 2002;15:268–274. [PubMed: 11891971]
8. Wild JM, Woodhouse N, Paley MN, Fichele S, Said Z, Kasuboski L, van Beek EJ. Comparison between 2D and 3D gradient-echo sequences for MRI of human lung ventilation with hyperpolarized 3He. Magn Reson Med 2004;52:673–678. [PubMed: 15334590]
9. Salerno, M.; Brookeman, JR.; Mugler, JP, III. High-Resolution Volumetric Imaging of the Lung Air Spaces using Hyperpolarized 3He and Spiral-Trajectory Pulse Sequences. Proceedings of the 9th International Society of Magnetic Resonance in Medicine; Glasgow, Scotland, UK. 2001. Abstract 943
10. Ruppert, K.; Miller, GW.; Altes, TA.; Mata, JF.; de Lange, EE.; Brookeman, JR.; Mugler, JP. Rapid hyperpolarized He-3 ventilation scanning with an optimized 3D acquisition scheme. Proceedings of the 13th International Society of Magnetic Resonance in Medicine; Miami Beach, Florida, USA. 2005. Abstract 2774
11. Ireland, RH.; Bragg, CM.; McJury, M.; Hatton, MQ.; Woodhouse, N.; Van Beek, EJ.; Wild, JM. The role of hyperpolarized 3He in MRI in NSCLC. Proceedings of the 14th Annual Meeting of ISMRM; Seattle, Washington, USA. 2006. Abstract 1662
12. Peters DC, Korosec FR, Grist TM, Block WF, Holden JE, Vigen KK, Mistretta CA. Undersampled Projection Reconstruction Applied to MR Angiography. Magn Reson Med 2000;43:91–101. [PubMed: 10642735]
13. Rasche V, Holz D, Proksa R. MR Fluoroscopy using projection reconstruction multi-gradient-echo (prMGE) MRI. Magn Reson Med 1999;43:324–334. [PubMed: 10440958]
14. Peters, DC.; Thompson, RB.; McVeigh, ER. Multi-echo projection reconstruction for real-time cardiac MRI. Proceedings of the 9th International Society of Magnetic Resonance in Medicine; Glasgow, Scotland. 2001. Abstract 1882
15. Barger AV, Block WF, Toropov Y, Grist TM, Mistretta CA. Time-Resolved Contrast-Enhanced Imaging With Isotropic Resolution and Broad Coverage Using an Undersampled 3D Projection Trajectory. Magn Reson Med 2002;48:297–305. [PubMed: 12210938]

16. Lu A, Brodsky E, Grist TM, Block WF. Rapid fat-suppressed isotropic steady-state free precession imaging using true 3D multiple-half-echo projection reconstruction. Magn Reson Med 2005;53:692–699. [PubMed: 15723411]

17. Brodsky, EK.; Lu, A.; Thorton, FJ.; Grist, TM.; Block, WF. Using multiple half-echos to improve efficiency and fat suppression in time-resolved MRA. Proceedings of the 11th International Society of Magnetic Resonance in Medicine; Toronto, Canada. 2003. Abstract 322

18. Mansfield P. Spatial mapping of the chemical shift in NMR. Magn Reson Med 1984;1:370–386. [PubMed: 6571566]

19. Wang SJ, Nishimura DG, Macovski A. Multiple-readout selective inversion recovery angiography. Mang Reson Med 1991;17:224–251.

20. Mugler JP III, Epstein FH, Brookeman JR. Shaping the signal response during the approach to steady state in three-dimensional magnetization-prepared rapid gradient-echo imaging using variable flip angles. Magn Reson Med 1992;28:165–185. [PubMed: 1461121]

21. Stehling MK. Improved signal in “snapshot” FLASH by variable flip angles. Magn Reson Imaging 1992;10:165–167. [PubMed: 1545677]

22. Sobering, GS.; Shiferaw, Y. Optimization of acquisition parameters for multi-shot hyper-polarized NMR: variable flip angle excitation. Proceedings of the 3rd International Society of Magnetic Resonance in Medicine; Nice, France. 1995. p. 687

23. Zhao L, Mulkern R, Tseng CH, Williamson D, Patz S, Kraft R, Walsworth RL, Jolesz FA, Albert MS. Gradient-echo imaging considerations for hyperpolarized 129Xe MR. J Magn Reson 1996;113:179–183.

24. Mugler, JP, III. Optimization of gradient-echo sequences for hyperpolarized noble gas MRI. Proceedings of the 6th International Society of Magnetic Resonance in Medicine; Sydney, Australia. 1998. p. 1904

25. Wild JM, Paley MNJ, Viallon M, Schreiber WG, van Beek EJR, Griffiths PD. k-space filtering in 2D gradient-echo breath-hold hyperpolarized ^{3}He MRI: spatial resolution and signal-to-noise ratio considerations. Magn Reson Med 2002;47:687–695. [PubMed: 11948729]

26. Miller GW, Altes TA, Brookeman JR, De Lange EE, Mugler JP. Hyperpolarized 3He lung ventilation imaging with B1-inhomogeneity correction in a single breath-hold scan. MAGMA 2004;16:218–226. [PubMed: 15108030]

27. Johnson GA, Cofer GP, Hedlund LW, Maronpot RR, Suddarth SA. Registered ^{1}H and ^{3}He magnetic resonance microscopy of the lung.

28. Wong, S.; Roos, M. Strategy for sampling on a sphere with applications to 3D selective pulse design. Proceedings of the 12th Annual Meeting of the SMRM; New York. 1993. p. 1178

29. Chen XJ, Moller HE, Chawla MS, Cofer GP, Driehuys B, Hedlund LW, Macfall JR, Johnson GA. Spatially resolved measurements of hyperpolarized gas properties in the lung in vivo. Part II: T_2* Magn Reson Med 1999;42:729–737.

30. Noll DC, Nishimura DG, Macovski A. Homodyne detection in magnetic resonance imaging. IEEE Trans Med Imaging 1991;10:154–163. [PubMed: 18222812]

31. Block, WF.; Peters, DC.; Vigen, KK. Homodyne reconstruction for projection reconstruction trajectories. Proceedings of the 7th International Society of Magnetic Resonance in Medicine; Philadelphia, Pennsylvania, USA. 1999. Abstract 659

32. Pipe JG. Reconstructing MR images from undersampled data: data-weighting considerations. Magn Reson Med 2000;43:867–875. [PubMed: 10861882]

33. Duyn JH, Yang Y, Frank JA, van der Veen JW. Simple Correction Method for *k*-Space Trajectory Deviations in MRI. Journal of Magnetic Resonance 1998;132:150–153. [PubMed: 9615415]

34. Brodsky, EK.; Block, WF. Characterization and correction of Gradient Errors. Proceedings of the ISMRM Workshop on Non-Cartesian MR; Sedona, Arizona, USA. 2007. Abstract

35. Mistretta CA, Wieben O, Velikina J, Block W, Perry J, Wu Y, Johnson K, Wu Y. Highly Constrained Backprojection for Time-Resolved MRI. Magn Reson Med 2006;55:30–40. [PubMed: 16342275]

36. Holmes, JH.; O’Halloran, RL.; Brodsky, EK.; Velikina, J.; Peterson, ET.; Block, WF.; Fain, SB. Imaging 3D respiratory dynamics using hyperpolarized He-3 multi-echo HYPR VIPR. Proceedings of Joint Annual Meeting ISMRM-ESMRMB; Berlin, Germany. 2007. Abstract 461

37. Pipe, JG.; Koladia, KV. Spiral Projection Imaging: a new fast 3D trajectory. Proceedings of the 13th International Society of Magnetic Resonance in Medicine; Miami Beach, Florida, USA. 2005. Abstract 2402

38. Deninger AJ, Eberle B, Ebert M, Grossmann T, Heil W, Kauczor H, Lauer L, Markstaller K, Otten E, Schmiedeskamp J, Schreiber W, Surkau R, Thelen M, Weiler N. Quantification of regional intrapulmonary oxygen partial pressure evolution during apnea by (3)He MRI. J Magn Reson 1999;141:207–216. [PubMed: 10579944]

39. Rizi RR, Baumgardner JE, Ishii M, Spector ZZ, Edvinsson JM, Jalali A, Yu J, Itkin M, Lipson DA, Gefter W. Determination of regional VA/Q by hyperpolarized 3He MRI. Magn Reson Med 2004;52:65–72. [PubMed: 15236368]

40. Wild JM, Fichele S, Woodhouse N, Paley MNJ, Kasuboski L, van Beek EJR. 3D volume-localized pO2 measurement in the human lung with 3He MRI. Magn Reson Med 2005;53:1055–1064. [PubMed: 15844148]

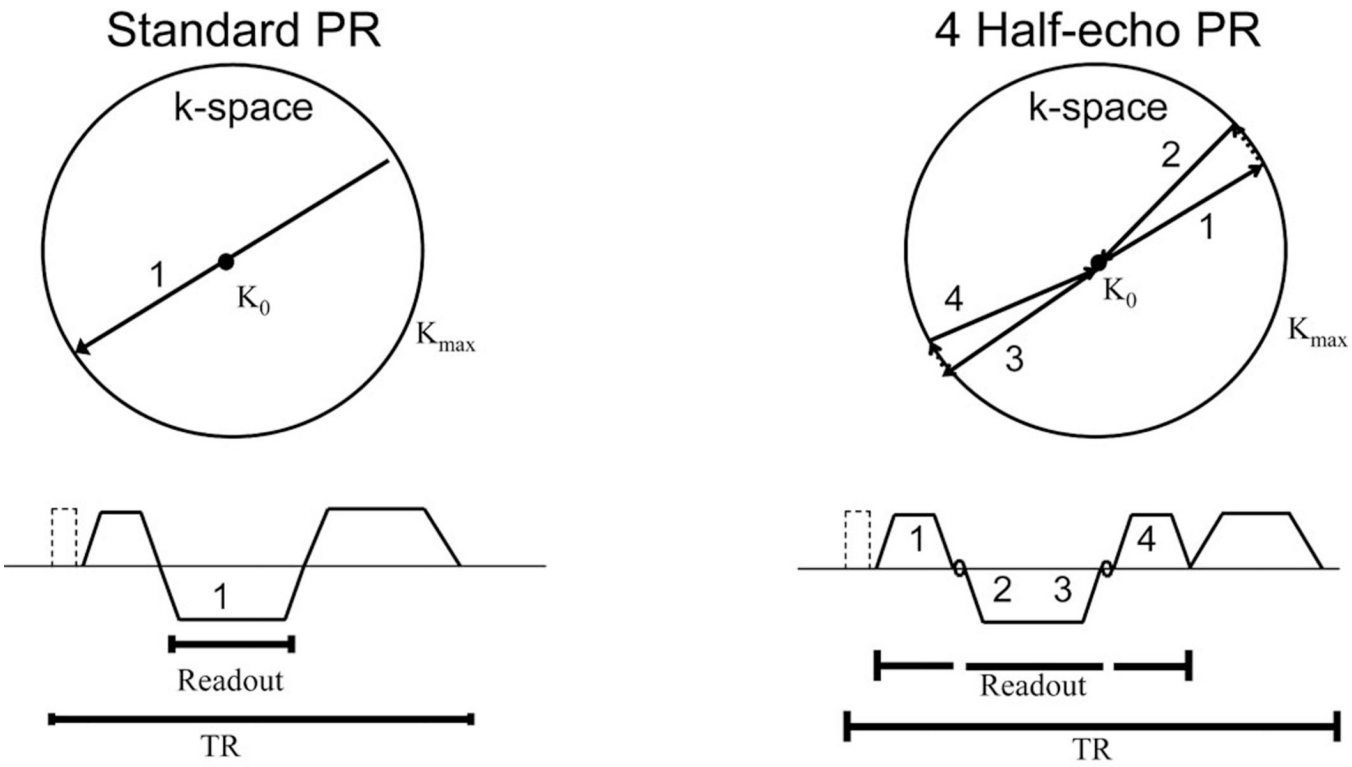

Figure 1.
An example of a 2 half-echo projection acquisition trajectory is shown beginning at the center of k-space, moving to the edge of k-space, making a small rotation in the angular position, and then returning to the center of k-space along a new projection angle. The accompanying pulse sequence diagram is shown below with the RF pulse and idealized gradients. The k-space trajectory for a 4 half-echo projection trajectory is also shown along with the corresponding pulse sequence diagram. Note the improved data collection efficiency in time.

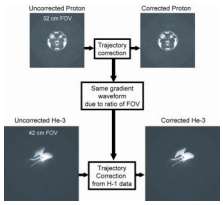

Figure 2.
Trajectory correction method demonstrating improved image quality for a bag filled with HP He-3. The isotropic delay between the RF chain and the data acquisition was found to be consistent between the proton system and the broadband. This allowed the use of a standard proton head phantom to map the true trajectory in k-space for the given gradient waveform used in the He-3 imaging experiments.

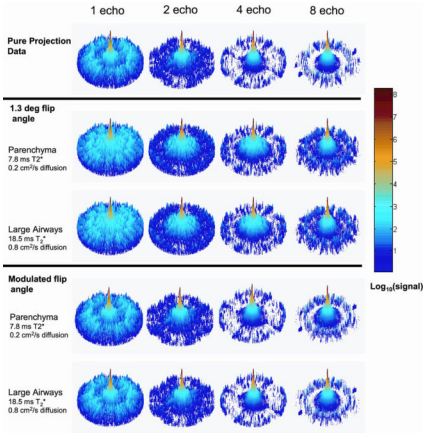

Figure 3.

Simulation results from PSF analysis for 20 s of data collection, using 1 half-echo, 2 half-echo, 4 half-echo, and 8 half-echo trajectories. Note each PSF is individually normalized to 1 and plotted as $\sqrt[4]{magnitude}$ to better depict the aliasing relative to each central peak (the amplitudes of the central peaks are reported in Table 2). With increasing numbers of half-echoes, the data collection efficiency is increased, resulting in suppression of the aliased energy and increased in the supported FOV in the PSF (a). Simulated signal decay from the constant RF flip angle, T_2* and diffusion in both the alveolar gas spaces and larger airways have relatively little effect on the side-lobes (b and c). The use of modulated flip angle with T_2* and diffusion, shows less degradation observed in the side-lobes (d, e) compared to the constant flip angle case (b, c).

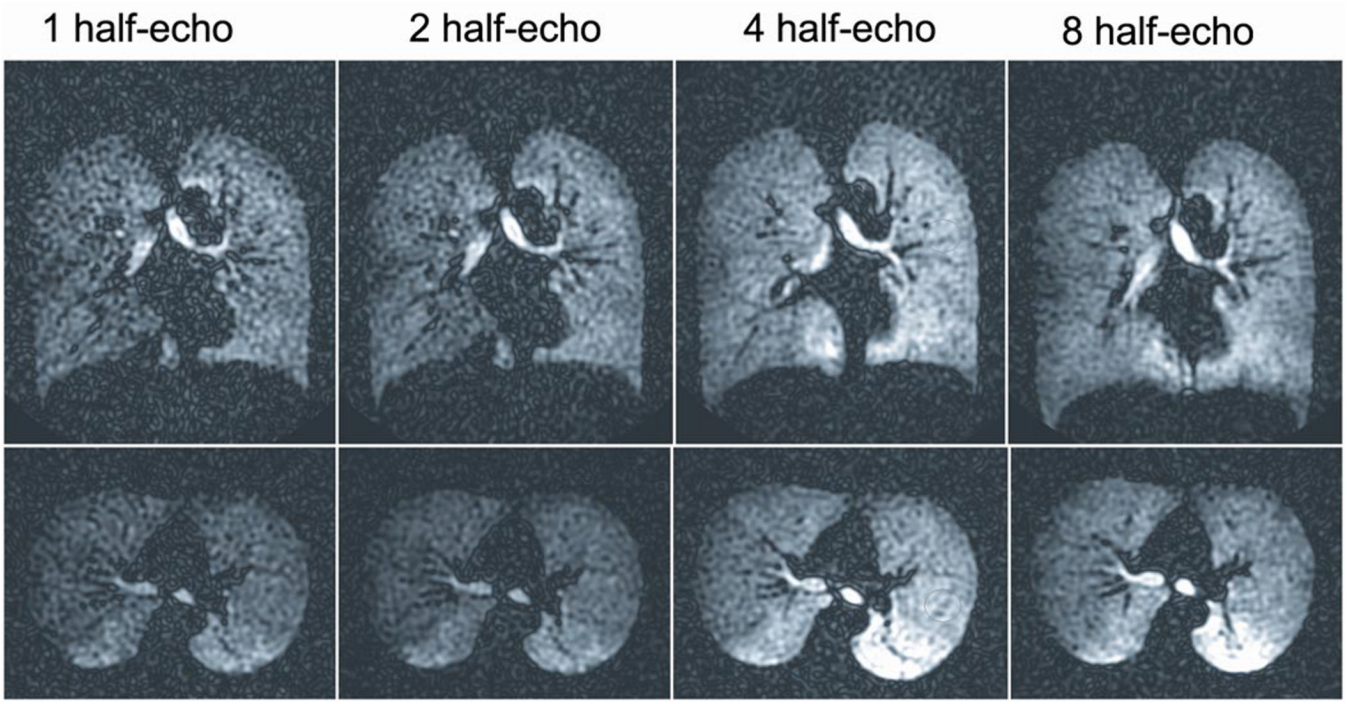

Figure 4.
Imaging results in the coronal and axial planes for multi-echo projection trajectories in separate volunteer studies using similar inhaled 5.6 mM HP He-3 doses, 20 s breath-holds, and modulated flip angles. Depiction of the He-3 signal is improved with the 4 and 8 half-echo trajectories compared to the 1 and 2 half-echo trajectories. The 8 half-echo trajectory allows further suppression of angular undersampling streak artifact compared to the 4 half-echo trajectory.

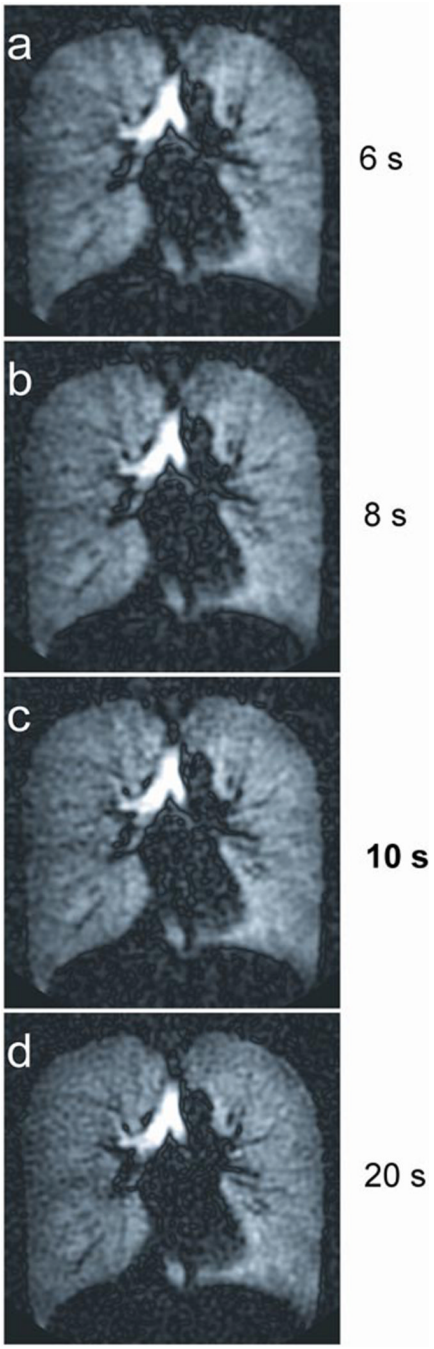

Figure 5.
Comparison of 3D reformats in the axial, coronal, and sagittal views from the 8 half-echo trajectory representing image acquisition times of 6 s, 8 s, 10 s, and 20 s, demonstrating the capability of this technique for adapting to shorter breath-hold times.

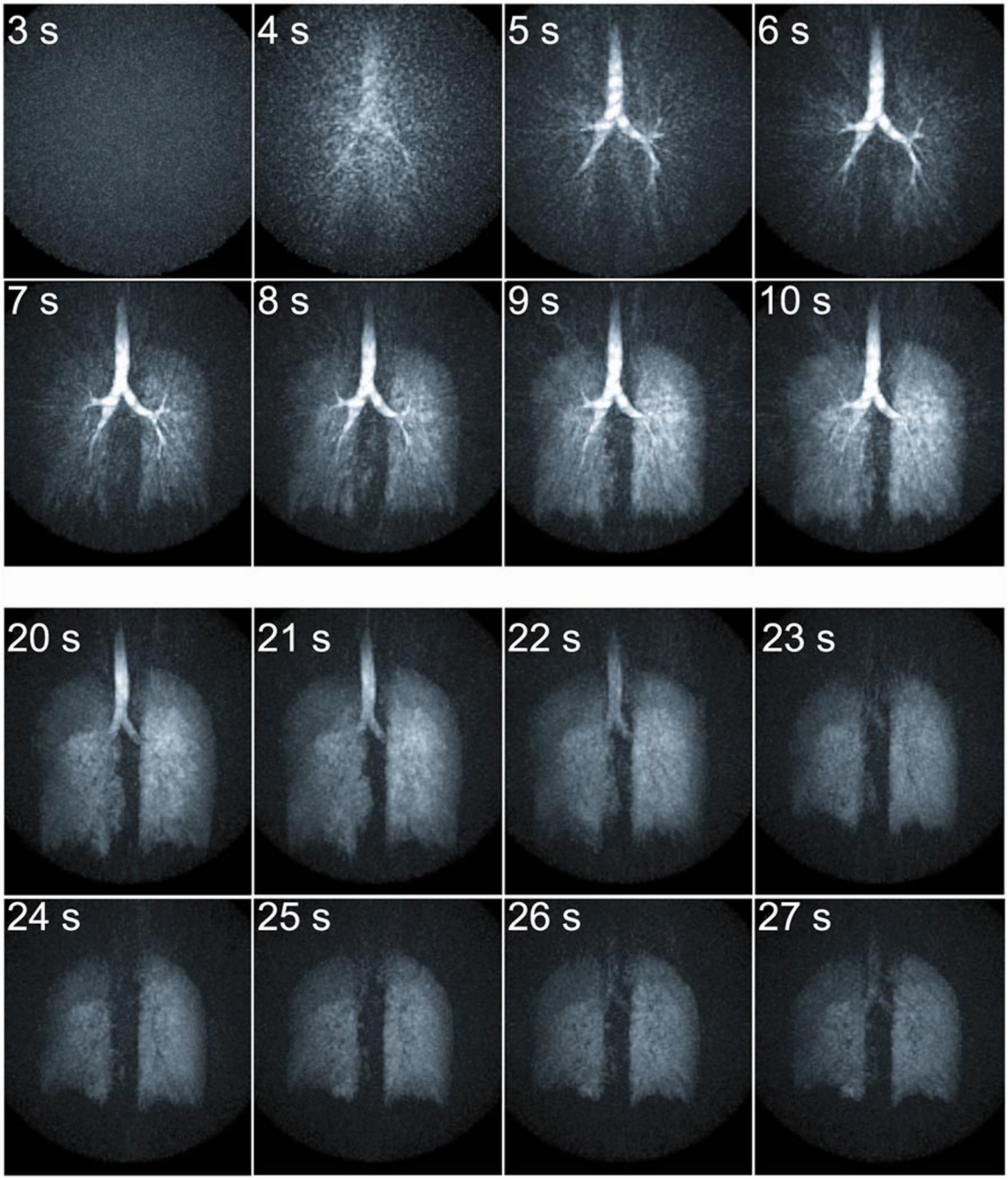

Figure 6.
Individual MIP images from a dynamic series of a respiration maneuver. Gas signal becomes visible in the large airways (4–6 s) followed by enhancement of the alveolar gas spaces (7–9 s). The breath-hold is depicted from 10–21 s. Finally upward motion of the diaphragm and loss of signal in the trachea are shown during forced expiration (22–25 s). The subject then held the forced exhale position (26 s).

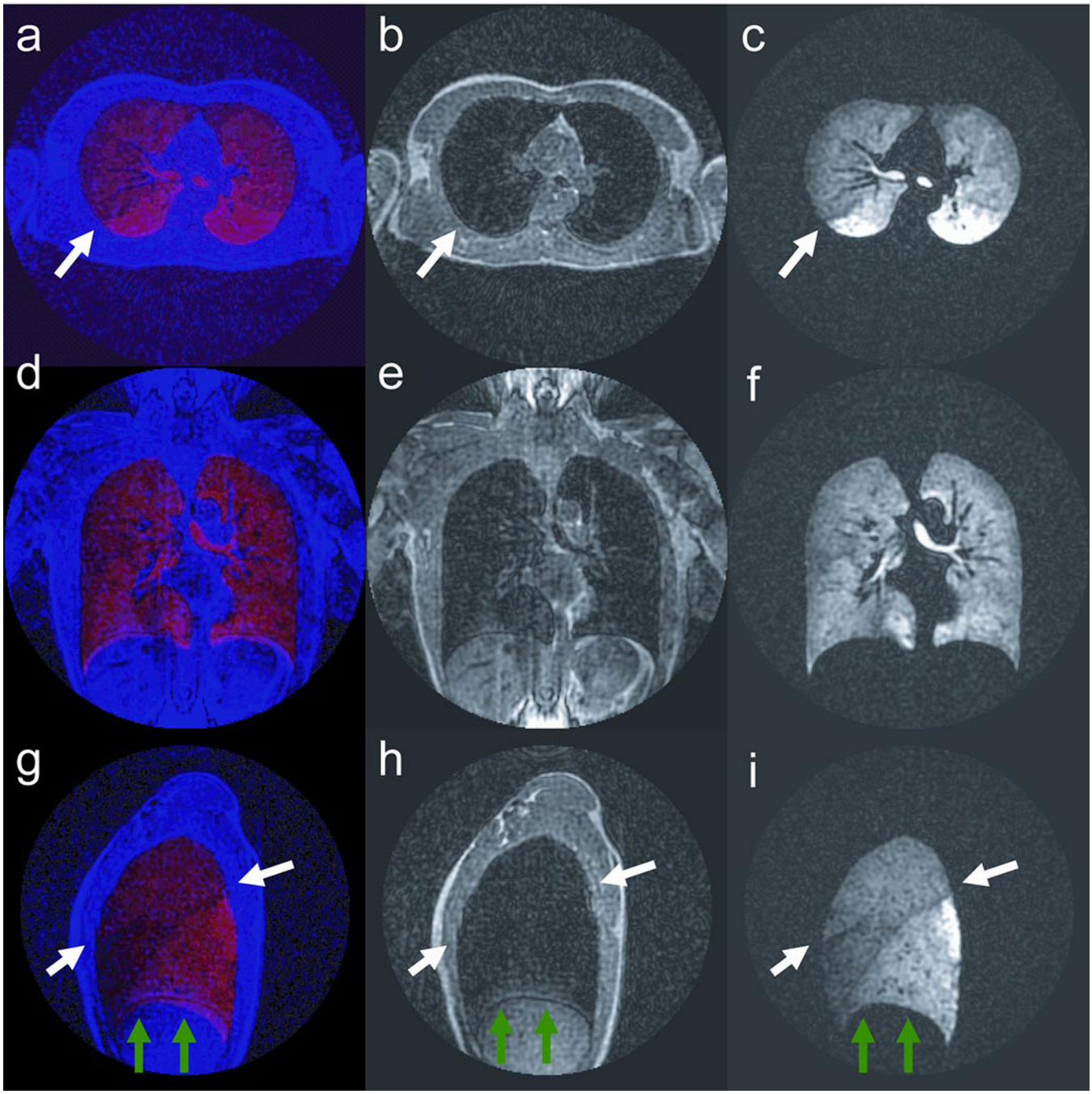

Figure 7.
Axial, sagittal, and coronal reformats of same 3D data sets shown in Figure 6 depicting inspiration (6 and 9 s), breath-hold (15 s), and following forced expiration (25 s). Delayed filling near a ventilation defect in the right middle lobe is visible (arrows).

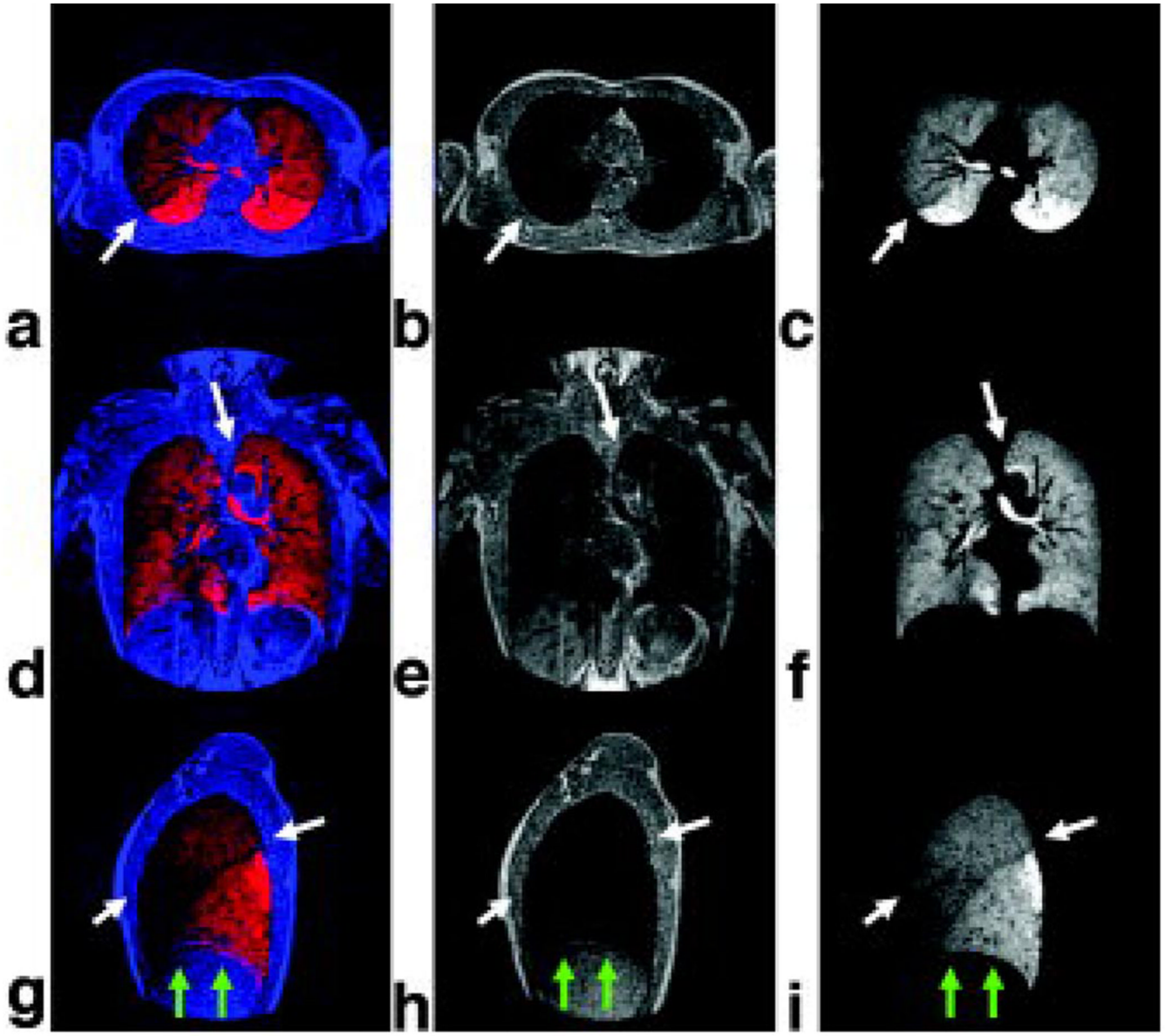

Figure 8.

Fusion images showing correspondence of He-3 ventilation (red) and proton anatomic structure (blue) (a, d, g) showing overlap of ventilation in the lung and pulmonary vasculature; and separate anatomic structure (b, e, h) and ventilation images (c, f, i). Note that separation of the lobes of the left lung is visible in the fused data and ventilation images, but not in the anatomic structure images. This confirms that signal modulation is not due to lung tissue (arrows, a, b, c). Sagittal fusion image (ventilation red, anatomic structure blue) depicting separation of the 3 lobes in the right lung (white arrows, g). Ventilation and anatomic structure were acquired in 2 separate breath-holds using the same volume of gas. Slight mismatch in the location of the diaphragm is visible (green arrows, g, h, i).

Table 1

Summary of acquisition parameters for the multi-echo trajectories and effective echo times when the center of k-space is sampled.

	1 Half-echo	2 Half-echo	4 Half-echo	8 Half-echo
TR (ms)	2.05	2.05	2.84	4.40
Sampled data points per TR	110	228	412	764
Total RF excitations in 20 s	8160	8160	6400	4400
Total projection angles sampled in 20 s	8160	16320	25600	35200
Half-echo Number	**1 Half-echo TE (ms)**	**2 Half-echo TE (ms)**	**4 Half-echo TE (ms)**	**8 Half-echo TE (ms)**
1	0.21	0.21	0.21	0.21
2–3		1.11	1.03	0.81
4–5			1.86	1.73
6–7				2.45
8				3.24

Table 2

Peak amplitude for PSF simulation results compared to SNR in volunteer studies for multi-echo PR acquisition trajectories.

Number of half-echoes		**1**	**2**	**4**	**8**
Simulation: constant flip angle					
Optimal constant flip angle (degrees)		1.0	1.0	1.1	1.35
PSF peak no T_2*, no diffusion		15.3	30.5	54.1	90.4
PSF peak for large airways		14.8	29.0	49.8	78.1
PSF peak for alveolar gas space		14.3	28.0	47.2	72.0
Simulation: modulated flip angle					
PSF peak no T_2*, no diffusion		16.9	33.8	59.9	100
PSF peak for large airways		16.4	32.2	55.1	86.5
PSF peak for alveolar gas space		15.8	31.0	52.3	79.7
Experiment: volunteer studies					
Trachea SNR	**Modulated flip angle**	22.5	30.2	30.2	40.8
	Constant flip angle				46.4
Alveolar gas space SNR	**Modulated flip angle**	2.0	2.6	7.4	10.3
	Constant flip angle				11.7